Korean J. Chem. Eng., 38(7), 1403-1415 (2021)
DOI: 10.1007/s11814-021-0805-5

pISSN: 0256-1115
eISSN: 1975-7220

The catalytic activity of Ce-Hf, Ce-Hf-Mg mixed oxides and RuO_2/HfO_2 deposited on CeO_2: Role of superoxide/peroxide in soot oxidation reaction

Hari Prasad Uppara*, Sunit Kumar Singh, Nitin Kumar Labhsetwar**, Mudiyaru Subrahmanya Murari***, and Harshini Dasari*,†**

*Department of Chemical Engineering, Manipal Institute of Technology, Manipal Academy of Higher Education, Manipal, 576104, India
**Energy and Resource Management Division, CSIR-National Environmental Engineering Research Institute, Nagpur, 440 020, Maharashtra, India
***DST-PURSE Program, Mangalore University, Mangalagangotri-574199, India
(*Received 28 January 2021 • Revised 23 March 2021 • Accepted 11 April 2021*)

Abstract−The synthesis of binary mixed oxide Ce-Hf (CH), ternary mixed oxide Ce-Hf-Ru (CHR), and Ce-Hf-Mg (CHM) has been attempted using the PVP-assisted sol-gel method. The structural and surface morphology of the prepared catalysts were investigated and studied for the generation of superoxides (O_2^-)/peroxides (O_2^{2-}) species and availability of lattice oxygen (O^-) during soot oxidation reactions. The successfully incorporated Hf^{4+}/Mg^{2+} into ceria (CH, CHM) enhances the redox potential sites on nano-flake morphology, thus produces more oxygen vacancies (□). However, Ru^{4+}/Hf^{4+} was not doped into the ceria structure in CHR catalyst; it showed lesser structural distortions generating fewer oxygen vacancies. In addition, it was observed that better performing catalysts should possess lower oxidation temperature and be catalytically stable. Indeed, the ternary oxide CHR featured excellent catalytic properties when compared with the others. However, CHM was found structurally and catalytically stable with self-regenerative capability even after the repeated soot oxidation experiments. Thus, the possible soot oxidation mechanism has been proposed on the prepared catalysts.

Keywords: Soot Oxidation, Superoxides/Peroxides, Catalytic Stability, Reaction Mechanism

INTRODUCTION

Many catalysts have been developed and studied for their physiochemical properties towards soot oxidation. They have been investigated for their feasibility in diesel particulate filters (DPF) to address its activity, environmental, and economic sustainability. A large number of studies on noble metal-based oxides [1], ceria based oxides [2], binary oxides [3,4], ternary oxides [5], perovskites [6,7], 3 DOM structures [8-10] have been reported, but still there is a need to explore more catalytic materials to meet the existing standards. Although the studies on noble metal-based oxides (Ru, Rh, Pd, Ag, and Pt) showed higher catalytic oxidation, they were not economically viable. Thus, alternative highly active non-noble metal-based oxides (Ce, Cu, Mn, Co, Ni) must be developed for catalysis applications.

The activity of the catalysts depends on the parameters like surface morphology of catalysts (nano-particles, nano-flakes, nanofibers, nanorods, etc.) [11-13] which are successively controlled by preparation methodology (sol-gel, hydrothermal, co-precipitation, etc.) [14]. The studies on the role of surface morphological properties towards soot oxidation are studied in the literature. For example, Cui et al. [13] studied that the nano-flake-based CeO_2 enhanced the soot oxidation activity, which provides more contact points for the soot with catalysts than nano-particle based CeO_2. Similar kinds of studies by Liu et al. [12] compared the oxidation studies over three morphological catalysts nano-cubes, nano-spindles, nano-particles based Ag/CeO_2. They concluded that Ag/CeO_2 (nano-cubic shaped) exhibited good catalytic performance for the oxidation of soot. Zhang et al. [15] reported the influence of different shapes of ceria (nanorods, nanocubes, nanoflakes) towards soot oxidation. They observed the activity was in the sequence of CeO_2-nanorods> CeO_2-nanoflakes>CeO_2-nanocubes. In similar studies reported by Bensaid et al. [16], the activity of different morphologies of CeO_2 was in the order of nano-powders>nano-fibers>nano-flakes=nano-sticks.

The soot oxidation over the catalysts prepared by different methods is also studied and reported in the literature. Piumetti et al. [5] synthesized the ternary oxides (Ce-Zr-Pr) using hydrothermal (NP) and solution combustion method (SCS) and applied them for soot oxidation applications. The authors concluded that the samples prepared through hydrothermal synthesis (nano-cube based $Ce_{0.8}Zr_{0.1}Pr_{0.1}O_2$, $T_{50\%}$=419 °C) exhibited higher catalytic activity than SCS method (polycrystalline agglomerates based $Ce_{0.8}Zr_{0.1}Pr_{0.1}O_2$, $T_{50\%}$= 444 °C). Recently, $Fe_{10}Ce_{90}$ were reported by Li et al. [17], who observed a sample prepared using the co-precipitation method ($T_{50\%}$= 377±2 °C) showed better oxidation activity than the solution combustion method ($T_{50\%}$=387±1.8 °C). Besides, the dispersant also plays a vital role in enhancing the properties of the catalyst; in particular, Hu et al. [18] described the addition of dispersants like PVP/PVA in synthesizing Pd supported catalysts. This enhanced the cata-

†To whom correspondence should be addressed.
E-mail: harshini.dasari@manipal.edu

lytic properties by improving the dispersion of Pd nanoparticles on the support and also inhibited the sintering of Pd species.

CeO_2 is recognized for oxygen storage/redox property and is widely used in catalysis applications [19]. The catalytic properties and thermal stability of CeO_2 can further be tuned by the substitution of foreign cations into the crystal lattice [20]. To date, many researchers have attempted to change the surface morphology and tried to create crystal defects in CeO_2 lattice: for example, Ce-Zr [21], Ce-Zr-Pr [5], Ce-Mn [22], Ce-Hf [23] enhanced the soot oxidation activity. Thus, non-noble metal based mixed metal oxides have attracted attention in the catalysis field, because of their higher activity, lower cost, and the possibility to accommodate different cations in the structure [24]. HfO_2 also exhibits good chemical and thermal stability under oxidizing conditions. However, the studies of HfO_2 towards soot oxidation were limited due to its low surface area, high density, and low porosity, but the surface area and nano-sized particles can be tailored with the help of dopants [25]. Anantharaman et al. [23] showed that doped Hf into fluorite phase CeO_2 enhanced the soot oxidation with $T_{50\%}$ measured as 430 °C, due to surface morphology/phase stability and availability of surface oxygen species. Ru and RuO_2 are well-known in the field of catalysis and relatively cheaper than other noble metals/oxides [26]. They suffer deactivation at higher temperatures (>800 °C) under oxidizing conditions, which leads to the formation of toxic RuO_3, RuO_4 gases but the Ru metal oxides can be stabilized with the help of different supports [27,28]. However, the present work focuses on the role of Ru towards soot oxidation at mild temperatures (<500 °C).

In this work, the soot oxidation on mixed metal oxides (Ce-Hf and Ce-Hf-Mg) and the un-doped composite oxide (Ce-Hf-Ru) was studied. The characterization techniques like XRD, FESEM/EDS, HR-TEM/SAED, Raman spectroscopy, XPS, O_2-TPD, H_2-TPR and soot-TPR analysis were used to understand the surface physio-chemical properties of the as-synthesized catalysts. In addition, we investigated the role of superoxide/peroxide species (formed via O_2 activation on the surface of prepared catalysts) towards soot oxidation and proposed the possible soot oxidation mechanism.

EXPERIMENTAL STUDIES

1. Synthesis of Catalysts

For the synthesis of binary oxide Ce-Hf (1 : 1 molar ratio), the ternary mixed oxides Ce-Hf-Mg and Ce-Hf-Ru (6 : 3 : 1 molar ratio), we modified the synthesis procedure as described by Cui et al. [13]. The following precursors obtained from Sigma-Aldrich and the samples were synthesized using PVP assisted sol-gel method: $Ce(NO_3)_3{\cdot}6H_2O$ (99% trace metals basis), $HfCl_4$ (98%), $RuCl_3{\cdot}xH_2O$ (99.98% trace metals basis), $Mg(NO_3)_2{\cdot}6H_2O$ (BioUltra, ≥99.0% (KT)), Polyvinylpyrrolidone (average molecular weight ~1,300,000 by LS) and citric acid monohydrate (≥99%). The required quantity of metal precursors was dissolved separately in 50 mL of deionized water. After that, the individual solutions were mixed together for 30 min to get a uniformly dispersed solution. Subsequently, PVP (weight ratio of PVP/metals was maintained as 1/1.5) was added slowly to the above-mentioned solution such that it was completely mixed with the metal solution. Here, PVP acts as a mild reducing agent and kinetically controls the growth of nano-particles [29]. Followed by the addition of citric acid to the solution by maintaining the molar ratios of citric acid to metals as 1.5 : 1. To the resultant solution, aqueous ammonia solution (28% NH_3 solution) is slowly added and the pH is maintained at around 10. Finally, the solution is dried at 90 °C and subsequently calcined at 700 °C/4 h.

2. Characterization of Catalysts

The phases formed in as-synthesized mixed oxides were analyzed by X-ray diffractometer equipment (Rigaku) using CuKα radiation (λ=1.54 A°). All the samples were recorded from 20 to 75° 2θ range at 2°/min. The size of crystals of the as-synthesized compounds was calculated using the Debye Scherrer equation. The particle morphology and microstructures of mixed oxides were observed by FESEM/EDS (Carl Zeiss, Germany) and TEM (Tecnai G2 20 (FEI) S-Twin with a point resolution of 0.24 nm and line resolution of 0.14 nm). For TEM analysis, the samples were sonicated and deposited on Cu-grid one day before the analysis. Raman spectra were recorded in Raman spectroscopy with PL analyzer (Airix Corp, STR 500, Japan) at room temperature with 532 nm wavelength of the laser beam. The spectra were taken from 200 to 4,000 cm^{-1} (resolution of <0.5 cm^{-1}). XPS spectra were recorded using ESCA+Omnicron nanotechnology apparatus with photon energy 1,486.6 eV of Al anode and Kα radiation. The XPS spectra were corrected using C1s peaks at 284.8 eV.

The temperature-programmed experiments (H_2-TPR and O_2-TPD) were studied using Micromeritics Auto Chem II 2920 instrument. H_2-TPR analysis provides information about reducibility and redox sites of the catalysts, while O_2-TPD gives data about the evolution of oxygen species from the surface of the catalyst. In H_2-TPR experiments, the sample was pretreated under Ar flow at 200 °C for 1 hr. Then the sample was cooled to 50 °C, subsequently, the sample was heated to 900 °C (5 °C/min) by exposing the sample to a gas flow of 10% H_2/Ar mixture (30 mL/min) to undertake the reduction process. The following experimental protocol was followed for O_2-TPD analysis. Initially, the physically adsorbed oxygen species was evacuated by heating the catalyst from 30 °C to 200 °C under inert He flows (30 mL/min) for 30 min. Subsequently, the gas was switched to O_2 flow (30 mL/min) and allowed to adsorb by the catalyst, followed by cooling to 50 °C and holding the sample under O_2 flow for 30 min. Then the gas was switched to inert He flows (30 mL/min) by heating the sample to 900 °C (5 °C/min); the desorbed oxygen species was detected by the TCD detector. Soot-TPR experiments were conducted to understand the availability of surface-oxygen species under an inert argon atmosphere (60 mL/min). In these experiments (TA instrument used), the soot/catalyst was mixed in the ratio of 1/10 under tight contact and heated in 50-700 °C temperature range at ramp input of 10 °C/min.

3. Catalyst Performance Studies

The performance of as-prepared catalysts towards carbon black was studied using a thermogravimetric analyzer. In these experiments, Catalyst : Printex U carbon black (Degussa) in the weight ratio of 10 : 1 was mixed thoroughly under tight contact for 5 min using an electric mortar and pestle. The mixed sample was activated under inert Argon flow (60 mL/min), followed by soot oxidation experiments under 5% O_2 (N_2 balanced) flow in the range of 50-700 °C at 10 °C/min, corresponding CO_2 profiles were collected using ACCURRA-S analyser with NDIR detector.

RESULTS AND DISCUSSION

1. X-ray Diffraction Technique

Fig. 1 reveals the XRD patterns of the CH, CHM, and CHR mixed oxides. From Fig. 1(a), it is evident that the binary oxide CH showed four significant diffraction peaks 29.3°, 33.9°, 48.7° and 57.9° corresponding to the planes (111), (200), (220), and (311), respectively. It was noticed that the smaller ionic size of Hf^{4+} (0.83 Å) was successfully doped into the cubic fluorite phase of CeO_2 (Ce^{4+}=0.97 Å) [30], and the peaks were well-matched with *Fm-3m(225)* space group (ICDD#03-065-5923), as well as with the literature [23,31, 32]. Similarly, the XRD of CHM is shown in Fig. 1(b), the smaller ionic sizes Hf^{4+} and Mg^{2+} (0.86 Å) cations were successfully substituted into the ceria lattice. Moreover, the major diffraction peak (111) was shifted to higher angles indicating the contraction of the lattice, as expected. The decrease in crystal size and the lattice param-

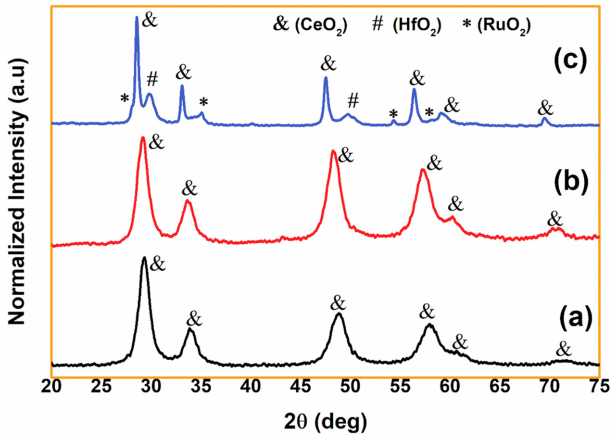

Fig. 1. XRD profiles of the as-prepared (a) CH, (b) CHM and (c) CHR.

Table 1. Crystal size and lattice parameter of the as-synthesized binary and ternary oxides

S. No	Catalyst	2θ (111)	d-Spacing (111) (Å)	Lattice constant (Å)	Cell volume (Å^3)	Crystal size (nm)	Lattice strain
1	CH	28.85	3.09	5.362	154.1	5.913	0.023
2	CHM	29.04	3.07	5.309	149.7	5.211	0.026
3	CHR	28.51	3.12	5.412	158.5	7.874	0.016

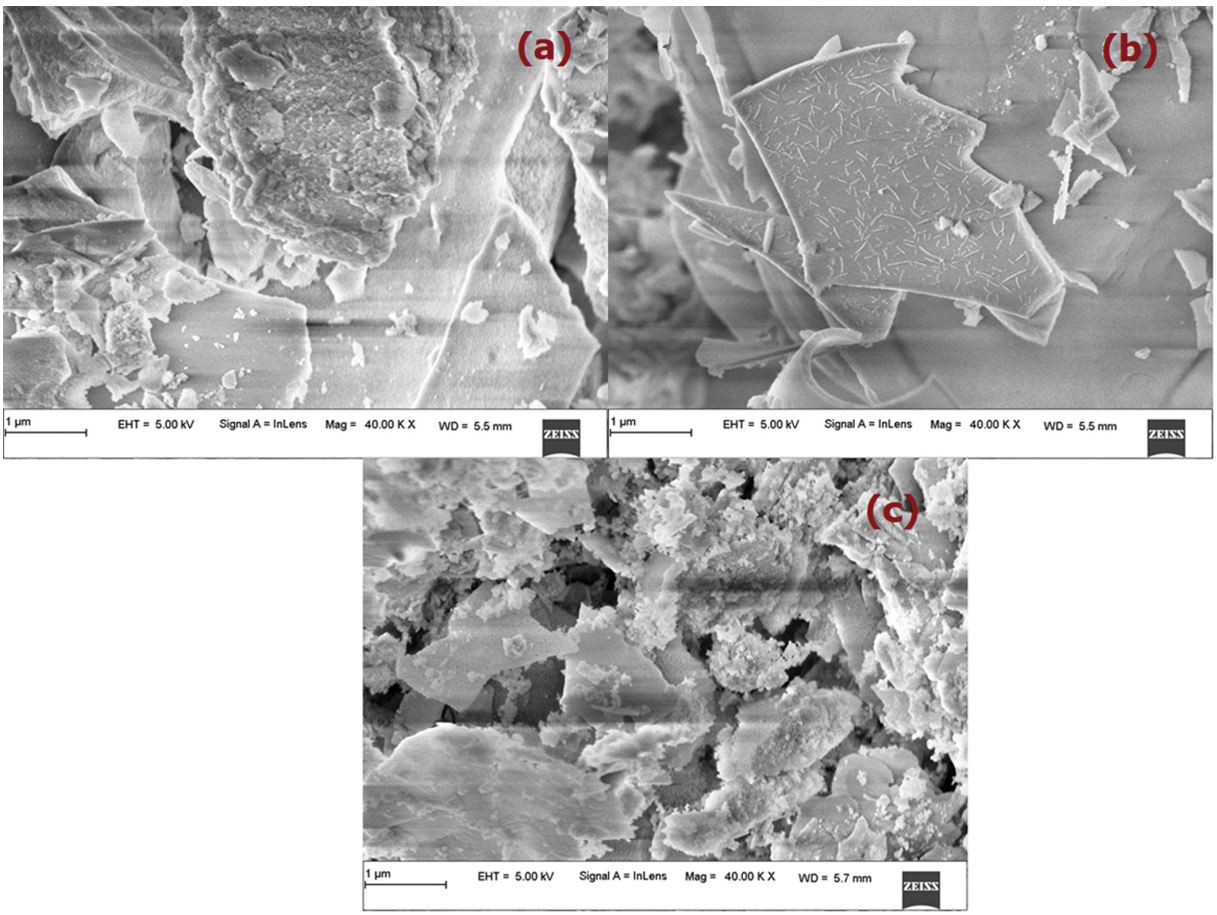

Fig. 2. FESEM images of the samples (a) CH, (b) CHM, and (c) CHR.

eter is shown in Table 1. The XRD profile of the CHR (Fig. 1(c)) shows the peaks for the secondary phases of HfO_2 (Orthorhombic phase, ICDD#00-021-0904) and RuO_2 (tetragonal phase, ICDD#01-075-4303) deposited onto the ceria surface because of significant differences in their ionic sizes. The foreign cation oxide (HfO_2) exhibited diffraction peaks at around 29.7° and 49.9°; and RuO_2 peaks exhibited at 28.0°, 35.1°, 54.3° and 58.1°, are consistent with the literature [33]. As shown in Table 1, the crystal size decreased, when it was attempted to substitute the larger ionic radius with the smaller ionic radii. In addition, the doped samples CH and CHM exhibited more structural strain as compared with the un-doped CHR.

2. Microscopic Techniques

2-1. FESEM Analysis

The morphology of the doped samples (CH and CHM) is observed to be nano-flake type as shown in Fig. 2(a), (b). This morphology can provide more external surface contact points with the soot. However, the un-doped CHR sample, as shown in Fig. 2(c), shows nanoparticle clusters of RuO_2/HfO_2 are observed outside of the nano-flake crystallites of CeO_2, well in accord with the XRD result. The elemental composition analysis of the samples is shown in Fig. S1 and Table S1.

2-2. TEM Analysis

The deposition of Ru/Hf species in the CHR sample is further confirmed by TEM analysis. As shown in Fig. 3(i), the RuO_2/HfO_2 nanoparticles are clearly visible outside of the CeO_2 nano-flakes, which is consistent with XRD and FESEM. Moreover, the particle sizes of RuO_2 and HfO_2 are found to be ~9 to 15 nm [34-36]. Indeed, the lattice fringes of CeO_2, RuO_2 and HfO_2 were captured from HRTEM and shown in Fig. 3(ii)-(iv). Based on the fast Fourier transform (FFT) technique, the interplanar distance of CeO_2 (111), RuO_2 (110) and HfO_2 (111) was calculated as 0.313, 0.319 and 0.297 nm, respectively, corroborating the XRD result (d=0.312, 0.317 and 0.294 nm, respectively), as well as with the literature [13]. Furthermore, the SAED pattern of the CHR sample is also recorded and shown in Fig. 3(v). It reveals that the sample exhibited a polycrystalline nature. Bright electron diffraction rings are observed and indexed to the cubic fluorite of CeO_2 (111), obtaining the d-spacing as 0.301 nm [37], which further supports the XRD result. In addition, large and small bright spots were indexed to phases of Ru and Hf oxides.

3. Spectroscopic Techniques

3-1. Raman Spectroscopic Analysis

Raman spectroscopy is used to investigate the concentration of oxygen vacancies (□) generated due to the creation of defective sites on the surface of the catalysts, shown in Fig. 4. According to the reported literature [19,38,39], the cubic-fluorite structure CeO_2 exhibits a Raman active F_{2g} (first-order scattering) mode at 465 cm^{-1}. Besides, the weak band at around 500-650 cm^{-1} [13] is related to second-order scattering caused because of oxygen vacancies produced by the partial reduction of Ce^{4+} to Ce^{3+}. In this work, the binary oxide CH showed an F_{2g} band at around 468.5 cm^{-1} that was consistent with the reported literature; in particular, Mukherjee et al. [32] reported F_{2g} at 469 cm^{-1} and Khder et al. [40] also observed at around 470 cm^{-1} for the mixed oxide $Ce_{0.8}Hf_{0.2}O_2$. Moreover, the CH sample blue-shifted F_{2g} mode towards higher wavenumber as compared with the CeO_2 (not shown in the figure, widely available

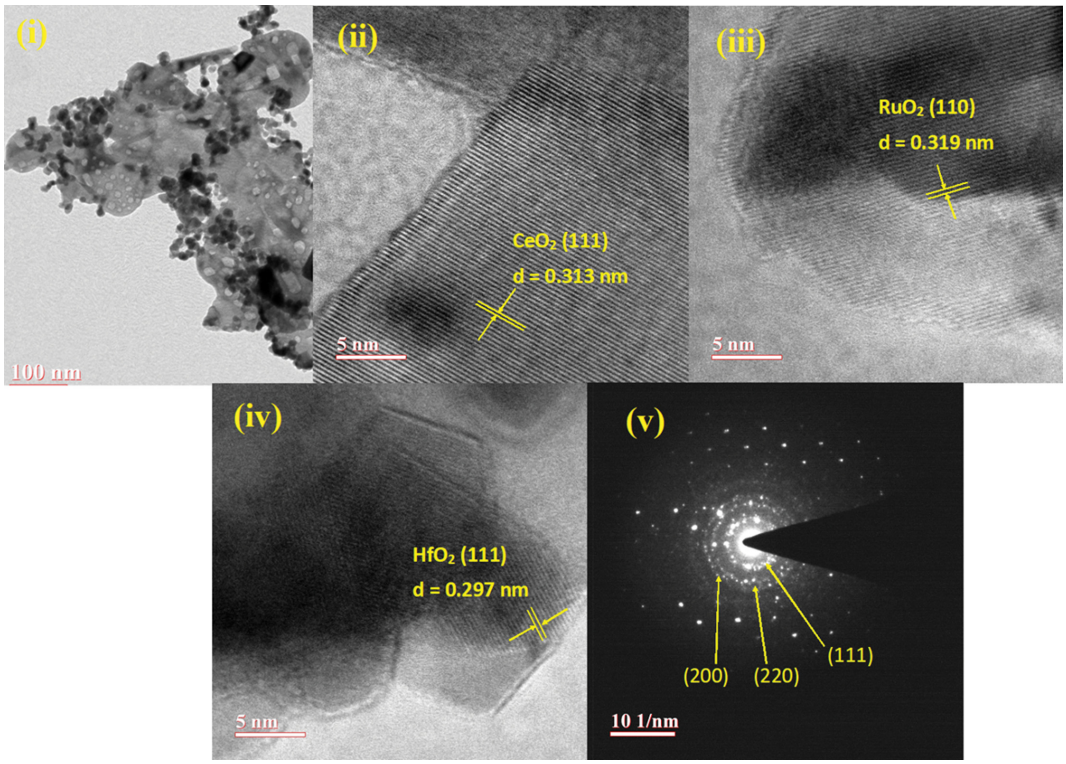

Fig. 3. TEM images of the CHR sample. (i) TEM image of deposited particles on CeO_2, (ii) HRTEM of CeO_2, (iii) HRTEM of RuO_2, (iv) HRTEM of HfO_2, (v) SAED pattern of CHR.

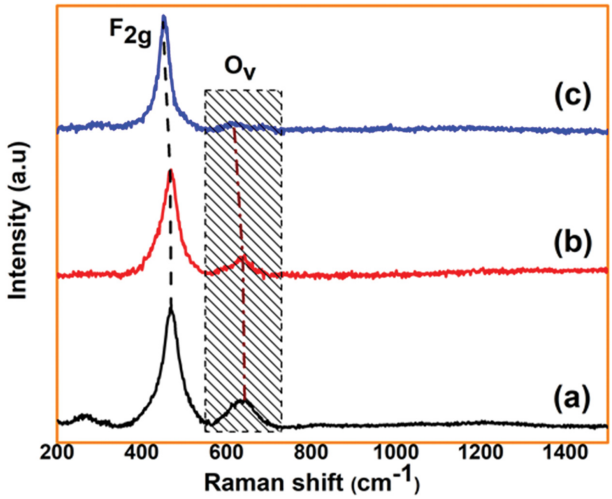

Fig. 4. Raman spectroscopic analysis of the as-prepared catalysts (a) CH, (b) CHM and (c) CHR.

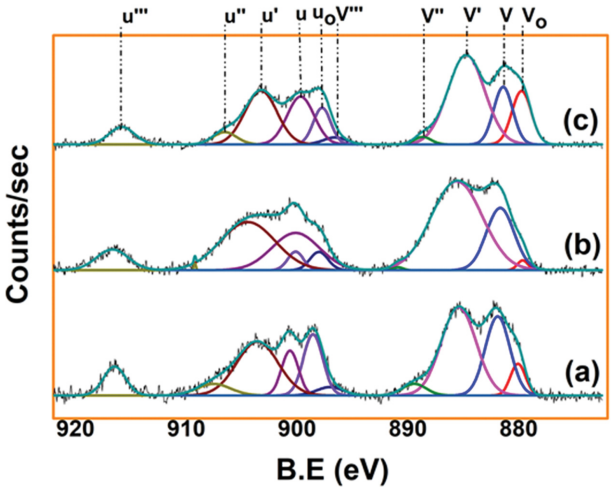

Fig. 5. XPS analysis of Ce3d of the as-prepared catalysts (a) CH, (b) CHM, (c) CHR.

in the literature), signifying the vibration of Ce-O bonding symmetry by the successful incorporation of smaller ionic size Hf^{4+} into CeO_2. The F_{2g} band for the ternary mixed oxides CHM and CHR showed at 465.6 and 452.5 cm^{-1} respectively, red-shifted towards lower wavenumber as compared with the binary oxide CH, labile structural strain in the lattice due to differences in their ionic sizes. Comparing the doped CH/CHM samples with un-doped CHR exhibited more lattice strain (shown in Table 1) which successively promotes the mobility of lattice oxygen, i.e., created more oxygen vacancies [32,37]. Besides, Raman shift for the doped CH/CHM samples evidenced a red-shift as compared with the un-doped CHR sample, which might due to lattice shrinkage because of successful incorporation of dopants [13].

Moreover, as reported in the earlier studies, the bands that appeared at around 528, 644, and 716 cm^{-1} were assigned to E_g, A_{1g}, and B_{2g} modes for the pure RuO_2 [41,42]. Interestingly, for the CHR sample, the bands of RuO_2 were not detected in the spectra, although it was deposited on the surface, which might be due to low-intensity peaks as compared with the F_{2g} band. In fact, Ledwa et al. [43] also did not notice the bands for RuO_2 for the sample $Ce_{0.95}Ru_{0.05}O_2$, and Satsuma et al. [44] also did not detect the bands for Ru/CeO_2 sample in Raman spectroscopy because of overridden F_{2g} peak of CeO_2.

The bands observed at 634.8, 633.6, and 618.9 cm^{-1} for the samples CH, CHM, and CHR, respectively, were related to vacancies generated due to the transformation of Ce^{4+} to Ce^{3+} (CeO_2 to CeO_{2-x}). The calculated peak area ratio (I_{V-o}/I_{F2g}) of the samples CH, CHM, and CHR was found to be 0.27, 0.13, and 0.04, respectively, signifying the binary oxide CH showed more oxygen vacancy concentration as compared with the ternary oxides (CHM and CHR). Here, the authors interpreted the decrease of oxygen vacancy formation in ternary mixed oxide CHM was due to the incorporation of isovalent cations (Hf^{4+}, Mg^{2+}) created fewer defective sites as compared with the binary oxide CH. It was consistent with the results reported by Vinodkumar et al. [45]; doping of isovalent Zr^{4+} cation into the ceria lattice exerted the structural distortion; however, limited oxygen vacancy concentration was observed on the surface. Moreover, CHR also exhibited fewer oxygen vacancies as compared with the doped CH and CHM samples because the foreign cations Ru^{4+}/Hf^{4+} deposited on the ceria lattice, therefore, induced relatively fewer structural defects compared with the other two samples.

3-2. XPS Analysis

Fig. 5 depicts the XPS spectra of Ce3d. The core levels of Ce3d spectra evidenced $Ce3d_{5/2}$ (labeled as 'V' in the figure) and spin-orbital contribution of $Ce3d_{3/2}$ (labeled as 'u'). For all the samples, the peaks identified at around ~880 eV (V_o) and ~885.4 eV (V^{I}) belong to trivalent $Ce3d_{5/2}$ with spin-orbital energy of trivalent $Ce3d_{3/2}$ located at around ~898.5 eV (u_o) and ~903.5 eV (u^{I}). Similarly, the tetravalent $Ce3d_{5/2}$ located at around ~881.9 eV, ~889.4 eV, ~897.0 eV are labeled as V, V^{II}, V^{III}, respectively, and the corresponding spin-orbital contribution of tetravalent $Ce3d_{3/2}$ are centered at ~900.6 eV (u), ~907.6 eV (u^{II}) and ~916.3 eV (u^{III}), all the peaks are well in accord with the literature [43]. Thus, all the samples possess both Ce^{3+} and Ce^{4+} cations on the surface; however, all the samples showed a higher amount of Ce^{3+} when compared with Ce^{4+}. Moreover, the reduction (R) of the ceria is calculated and shown in Table S2. The R-values for the samples CH, CHM and CHR were obtained as 0.62, 0.63 and 0.66, respectively. It signifies all the samples exhibited higher amount of lower valence cation Ce^{3+} than Ce^{4+}.

The XPS of Hf4f peaks (shown in Fig. 6(i)) located at around 16.5±0.5 eV and 18±0.5 eV are related to Hf^{4+} $4f_{7/2}$ and Hf^{4+} $4f_{5/2}$, respectively. Fig. 6(ii) depicts the core level Mg1s spectra of CHM sample and the peak is centered at around 1,303.2 eV, indicating the sample contains Mg^{2+} cations on the surface [46]. In CHR, the peaks of Ru3d and C1s are shown in Fig. 6(iii)-(iv). The Ru^0 peaks are located at around 279.4 eV ($Ru3d_{5/2}$) and 283.6 eV ($Ru3d_{3/2}$) with a spin-orbit energy difference of 4.0 eV. Similarly, the peaks centered at around 280.2 eV and 285.1 eV are ascribed to Ru^{4+} $3d_{5/2}$ and Ru^{4+} $3d_{3/2}$, respectively, with spin-orbit energy difference of 4.9 eV [43]. The ratio of Ru^0 to (Ru^0+Ru^{4+}) is obtained as 0.066, indicating the composition of Ru^{4+} is much higher than the metal-

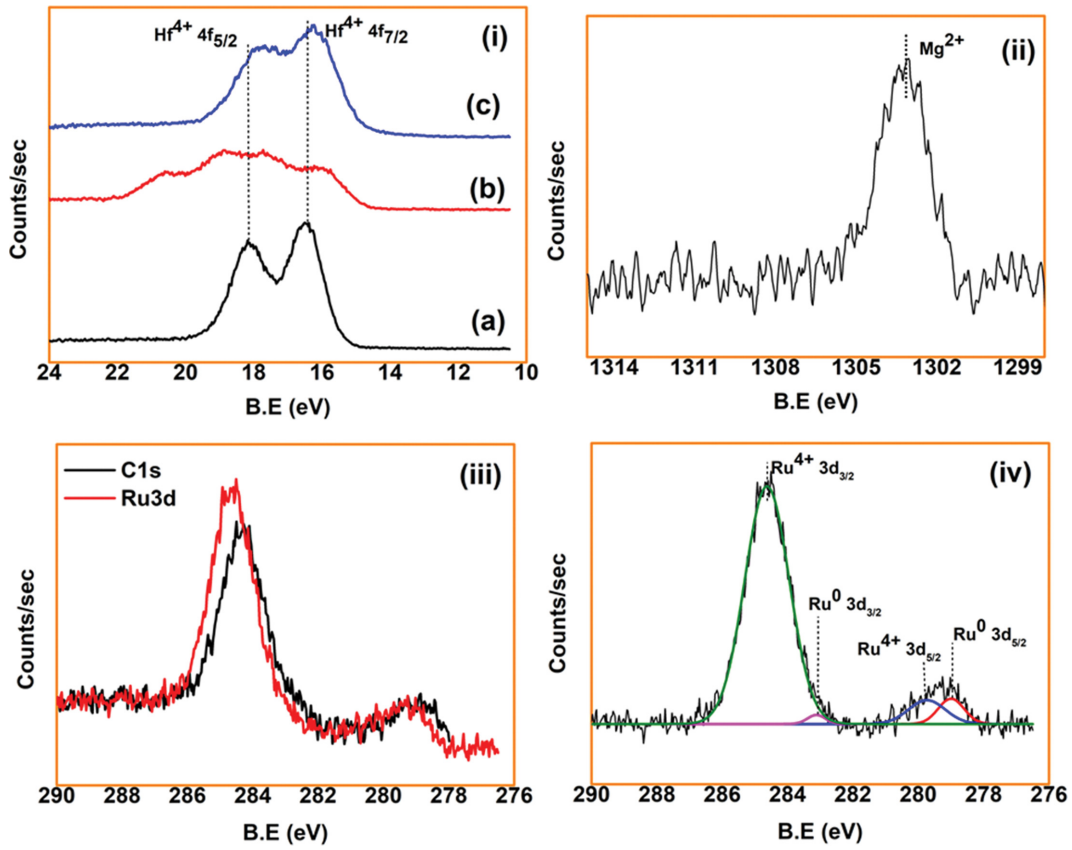

Fig. 6. (i) XPS analysis - Hf4f of the compounds (a) CH, (b) CHM, (c) CHR; (ii) XPS of Mg1s; (iii-iv) XPS of C1s and Ru3d.

lic Ru.

4. Temperature Programmed Analysis

4-1. H_2-TPR Analysis

The reducibility of the as-synthesized catalysts is often attributed to the activity of the catalyst. In general, the reduction peaks are divided into two kinds: (i) lower temperature reduction occurs at below 500 °C, indirectly associated with the release of superoxide/peroxide, and (ii) higher temperature reduction peak at above 500 °C is related to desorption of lattice oxygen species. In this work, the complete reduction process for all the samples was observed below 500 °C. The profiles are shown in Fig. 7 and the corresponding peak temperatures and H_2-Consumed are shown in Table 2. According to the literature [45,47,48], the pure CeO_2 exhibit a lower temperature reduction peak at 350-550 °C ascribed to the reduction of Ce^{4+}, which promotes the surface adsorbed oxygen O_2^-/O_2^{2-} and the higher temperature reduction peak usually occurs at 700-900 °C because of the reduction of bulk ceria (desorb O^{2-}). In the CH sample, we observed only one reduction peak at around 446 °C. It is attributed to the surface reduction of ceria Ce^{4+} to Ce^{3+} ($2CeO_2+H_2 \rightarrow Ce_2O_3+H_2O$); during the reduction process the oxygen atom is removed from the crystal lattice and creates an oxygen vacancy, as already evidenced in Raman spectroscopy. Thus, the substitution of smaller ionic size Hf^{4+} into the ceria lattice induces structural defects, consistent with the result obtained by Vinodkumar et al. [45]. While the three reduction peaks exhibited by the CHM sample are related to the ceria: the peaks exhibited at around 321 °C and 407 °C were assigned to reduction of easily reducible surface cerium or the outermost layer (together H_2 consumed quantity= 0.54 mmol·g^{-1}) and the peak exhibited at little higher temperature 479 °C is attributed to the reduction of innermost ceria (0.49 mmol·g^{-1}), which is consistent with the reported literature [49]. Moreover, MgO did not show any hydrogen reduction within the investigated temperature [50].

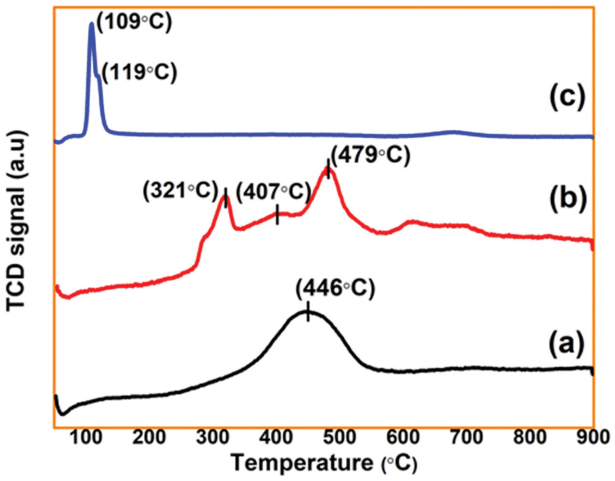

Fig. 7. The reducibility behavior of the catalysts (H_2-TPR): (a) CH, (b) CHM and (c) CHR.

Table 2. H_2 consumption of the as-prepared catalysts

S. No	Sample	Peak temperature (°C)	H_2 consumed (mmol·g^{-1})	Total H_2 consumed (mmol·g^{-1})
1	CH	446	0.66	0.66
2	CHM	321	0.25	1.03
		407	0.29	
		479	0.49	
3	CHR	109	0.52	0.77
		119	0.25	

As reported elsewhere [49], the RuO_2 showed reduction peaks between 60-150 °C. In the present study, CHR exhibited two peaks at around 109 and 119 °C; the first reduction peak was ascribed to the reduction of surface Ru and the second peak was due to the reduction of surface ceria around Ru species, in accord with the literature [41,51,52].

5. Role of Superoxides (O_2^-) and Peroxides (O_2^{2-}) in Reactions

5-1. O_2-TPD Analysis

O_2-desorption peaks are shown in Fig. 8 and the corresponding quantity of desorbed oxygen species is displayed in Table 3. In this technique, the three types of oxygen peaks are differentiated to characterize the behavior of catalysts. (i) Weakly bounded/physically adsorbed oxygen species (O_w) found at below 200 °C, (ii) Surface-chemisorbed oxygen species, i.e., superoxides (O_2^-) and peroxides (O_2^{2-}) detected in between 200-500 °C and (iii) lattice-oxygen species (O^{2-}) observed at above 500 °C [53]. According to the Mars-van-Krevelen mechanism, the surface chemisorbed oxygen species (O_2^-)/(O_2^{2-}) produced from the catalyst surface at below 500 °C due to the reduction of Ce^{4+} to Ce^{3+} was consumed by the activated soot particles and released the exhaust gases (CO_x), leaving the vacancy on the surface of the catalyst. Further, this vacancy was regenerated by the molecular oxygen species of the catalyst via re-oxidation of Ce^{3+} to Ce^{4+}. At above 500 °C, the oxidation process utilizes the lattice oxygen species produced by the catalyst.

In the present study, all the samples exhibited a strong peak at around ~60 °C, ascribed to weakly bounded oxygen species, which would not be involved in the oxidation process. Indeed, the most catalytically active of the catalysts (O_2^- or O_2^{2-}) are characterized based on the amount of oxygen desorbed between 200-500 °C. The total quantity of actively participating O_2^- or O_2^{2-} for soot oxidation reactions was found to be 0.028, 0.168, and 0.067 mmol·g^{-1} for the samples CH, CHM, and CHR, respectively. Thus, ternary mixed oxide showed higher surface-adsorbed oxygen species than binary oxide. Comparing the amount of active surface oxygen species between CHM and CHR ternary samples, CHR showed fewer O_2^- or O_2^{2-} species than the CHM sample. It is because the deposited RuO_2/HfO_2 on the CeO_2 surface that might lower the migration of surface oxygen species from CeO_2. The result was consistent with Dai et al. [54]; the Ru/CeO_2 showed fewer surface oxygen species when compared with pure CeO_2, due to the dispersion of Ru on the surface.

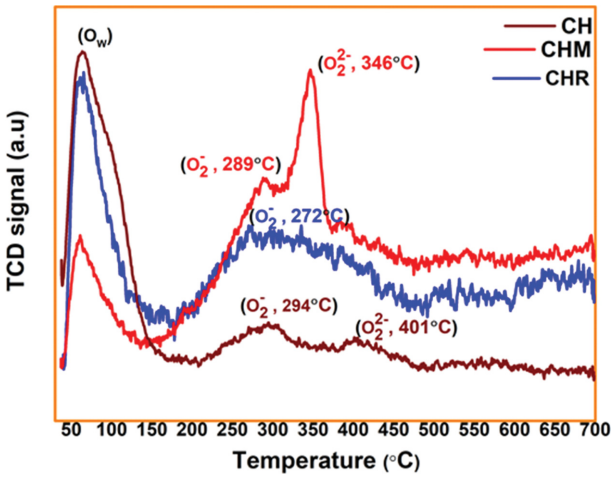

Fig. 8. O_2-TPD analysis of the as-synthesized catalysts.

Based on H_2-TPR and O_2-TPD, the temperature-programmed

Table 3. Temperatures - amount of active oxygen species obtained from O_2-TPD analysis

S. No	Sample	Temperature (°C)	Quantity (mmol·g^{-1})	Quantity of O_2^- (mmol·g^{-1})	Quantity of O_2^{2-} (mmol·g^{-1})	Total quantity of (O_2^-), (O_2^{2-}) (mmol·g^{-1})
1	CH	64	0.111	0.019	0.009	0.028
		294	0.019			
		401	0.009			
2	CHM	61	0.046	0.071	0.097	0.168
		289	0.071			
		346	0.097			
3	CHR	61	0.066	0.067	-	0.067
		272	0.067			

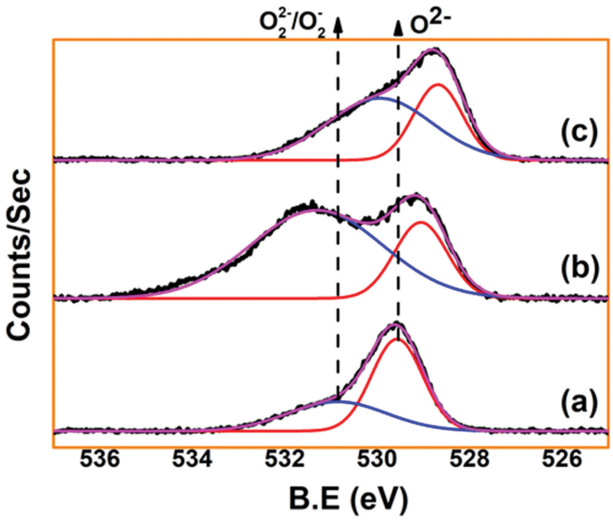

Fig. 9. O1s peaks of the as-prepared catalysts (a) CH, (b) CHM and (c) CHR.

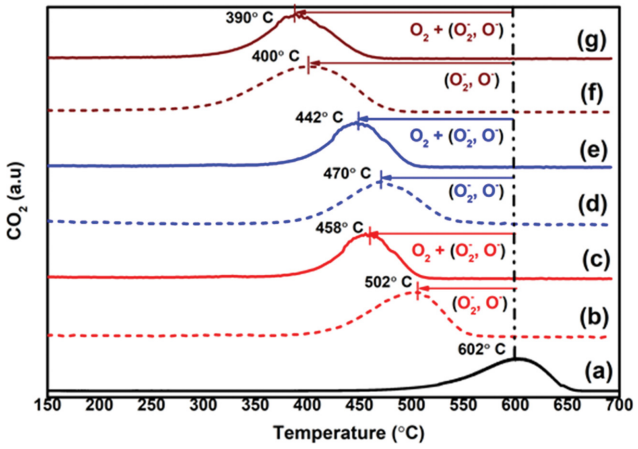

Fig. 10. Soot oxidation experiments over the catalyzed samples (a) Bare soot, (b)-(c) CH, (d)-(e) CHM and (f)-(g) CHR in the absence and presence of molecular oxygen species.

parameter (ξ_value) is defined as the sum of the amount of (O_2^-, O_2^{2-}) released from the catalyst and the amount of H_2 consumed due to the reduction of cations and the corresponding values are shown in Table 5. This parameter is used to evaluate the catalytic behavior for any oxidation reactions. The higher ξ_value signifies the higher catalytic activity of the samples. In this study, the reduction of Ce^{4+} and Ru^{4+} promotes the surface oxygen vacancies, consequently enhancing the oxygen storage capacity of the catalysts. Thus, ξ_value is directly proportional to the reduction of the cations and also the oxygen storage capacity of the catalyst. Among the catalysts, the ternary mixed oxides CHM and CHR exhibited higher ξ_values than the binary oxide CH. Thus, the samples CHM and CHR are catalytically active compounds for soot oxidation reactions.

5-2. XPS-O1s Analysis

The two peaks are distinguished in O1s and depicted in Fig. 9. The peak identified at around 529±0.5 eV is related to lattice-oxygen species O^{2-} and the peak located at around 530±0.5 eV is related to surface-chemisorbed oxygen species O_2^{x-} which are indirectly formed due to the redox potential of neighboring elements (Ce, Ru) and also the availability of surface vacancies. In general, the ratio O_2^{x-}/O^{2-} (shown in Table 4) is used to evaluate the catalyst performance. It means the catalyst should possess a higher quantity of O_2^{x-} species for any oxidation reactions. Thus, the ternary mixed oxides have shown higher catalytic activity because of the higher ratio of O_2^{x-}/O^{2-} (CHM=2.88 and CHR=1.75) when compared with the binary oxide (CH=0.61). Besides, comparing the amount of reactive anions O_2^{x-} between CHR and CHM, the sample CHM shows a higher amount because successful incorporation of foreign cations into the lattice promoted good redox potential sites and more surface vacancies; the results are well corroborated with Raman, H_2-TPR, and O_2-TPD.

5-3. Presence and Absence of Molecular Oxygen in Soot Oxidation

To investigate the role of superoxides and peroxides towards soot oxidation under two different atmospheres, we conducted two different experimental protocols. In the first experimental study, the soot-TPR analysis was performed under the inert atmosphere (Ar flow, 60 mL·min^{-1}) in which the soot itself acts as the reductant and the corresponding CO_2 evolution profiles are presented in Fig. 10(b), (d), (f). The T_{max} values for the samples CH, CHM, and CHR were measured as 502, 470, and 400 °C, respectively. It was noticed that the T_{max} values decreased by around 100, 132, and 202 °C for the samples CH, CHM, and CHR, respectively, as compared with un-catalyzed soot. The decrease in soot oxidation temperature for CH/CHM was due to the redox potential of ceria oxide (Ce^{4+}/Ce^{3+}) promoted to migrate lattice oxygen O^{2-} (evidenced in XPS) to the surface vacancies. Although, CHR evidenced fewer surface vacancies, but it exhibits lower oxidation temperature due to the lower redox potential of RuO_2.

In the second experimental protocol, the soot oxidation reactions were performed under the flow of bulk air (5% O_2+N_2 (bal-

Table 4. Reactive oxygen species and the corresponding binding energy (XPS analysis)

S. No	Sample	B.E (eV)	Area	FWHM	Ratio of O^{2-}/O_2^{x-}	Ratio of O_2^{x-}/O^{2-}
1	CH	529.56	7,953.08	1.299	1.62	0.61
		530.86	4,881.71	2.500		
2	CHM	529.05	4,406.28	1.346	0.34	2.88
		531.30	12,720.24	3.354		
3	CHR	528.68	6,593.80	1.239	0.57	1.75
		529.90	11,543.01	2.646		

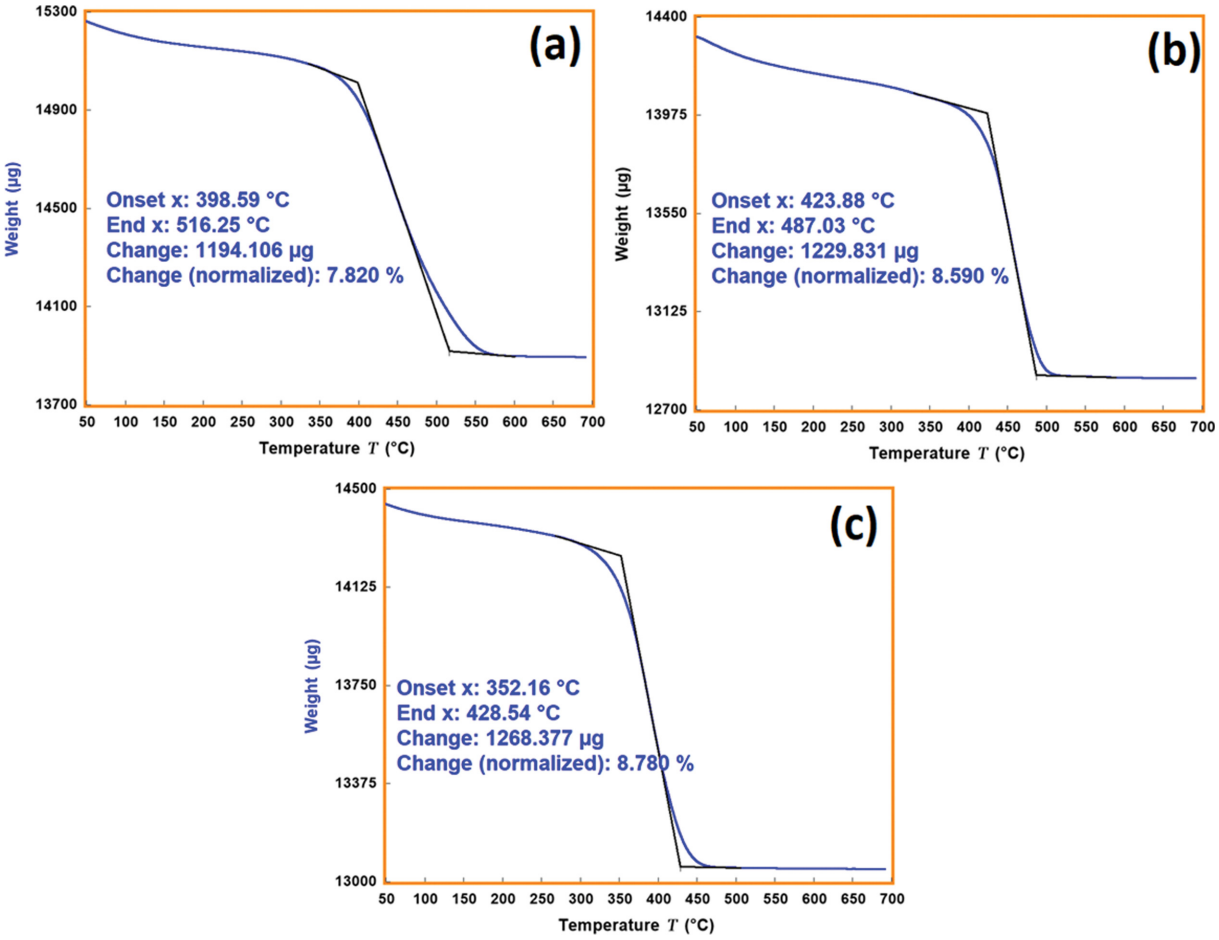

Fig. 11. Soot oxidation experiments over as-prepared mixed oxides (a) CH, (b) CHM and (c) CHR.

Table 5. The soot oxidation temperatures measured under 5% O_2+N_2 atmosphere

S. No	Sample	T_o (°C)	T_f (°C)	ΔT (°C)	T_{max} (°C)	ξ_value (mmol·g^{-1})
1	CH	399	516	117	458	0.688
2	CHM	424	487	63	442	1.198
3	CHR	352	429	77	390	0.837
4	Bare soot	552	627	75	602	-

ΔT=Final temperature - Onset temperature.

anced)) and the corresponding profiles are displayed in Fig. 10(c), (e), (g) with the dotted lines. In this study, the gaseous molecular oxygen species (O_2) was activated by the formation of surface chemisorbed oxygen species [(O_2^-), (O_2^{2-})], which further promoted the soot oxidation reactions. The T_{max} values in these experiments decreased by around ~150-200 °C for all the samples when compared with the un-catalyzed soot. In this study, the contribution of gaseous oxygen species (O_2) helped to boost the formation of O_2^- or O_2^{2-} species, which enhanced the oxidation of the soot. Comparing the presence of gaseous oxygen-rich species with the absence of O_2, the T_{max} values decreased by 44, 28, and 10 °C for the samples CH, CHM, and CHR respectively. Thus, the superoxide/peroxide played an important role in the soot oxidation reactions. However, these activated molecular oxygen species showed a relatively lesser contribution in the case of CHR with a temperature decrease of ~10 °C.

6. Catalyzed Soot Oxidation Experiments

The oxidation of soot over the binary mixed oxides (CH) and the ternary oxides (CHM and CHR) under tight contact mode is presented in Fig. 11. The corresponding temperature at which soot started to ignited is referred to as onset temperature T_o, and the complete soot oxidation temperature represented as T_f is displayed in Table 5. The difference between T_o and T_f is noted as ΔT, which signifies the temperature required for complete oxidation of soot. The catalyzed soot samples exhibited a significant decrease in onset temperature as compared with the bare soot. It is noticed that the T_{max} values decreased by around 144, 160, and 212 °C of the samples CH, CHM, and CHR, respectively, as compared with the un-catalyzed soot. This significant decrease in maximum soot oxidation temperature is due to the release of the higher content of

surface adsorbed oxygen species and the lower temperature reduction behavior of the catalysts enhanced the soot oxidation activity. Moreover, the temperature difference between onset and the end temperature (ΔT) was found to be 117, 63, and 77 °C for the samples CH, CHM, and CHR, respectively.

The temperature-programmed parameter (ξ_value) should be correlated with the soot oxidation activity. The higher ξ_value signifies the higher soot oxidation rate. The ξ_values for CHM and CHR samples were obtained as 1.198 and 0.837 mmol·g^{-1}, respectively. The higher ξ_value for CHM was due to more lattice strain (evidenced by XRD) followed by the creation of more oxygen vacancies (evidenced by Raman), higher migration of surface-active oxygen species and good reduction properties as compared with RuO_2/HfO_2 deposited CHR sample (shown in Table 2 and Table 3). As expected, CHM should show better oxidation activity than CHR; on the contrary, CHR (390 °C) showed the least maximum soot oxidation temperature than CHM (442 °C). This was due to deposited RuO_2 and weaker interactions of Ce-O-Ru interfaces promoted more activity in the first cycle of reaction. Furthermore, to confirm this activity catalytic stability studies were carried out for better understanding the catalyst.

7. Catalytic Stability Studies

Fig. 12 shows the catalytic stability of the ternary mixed oxides, the catalyzed soot samples tested for five cycles of soot oxidation reactions, and the corresponding T_{max} values are presented in the inset graph. The maximum soot oxidation temperature difference between the first cycle and fifth cycle of CHM and CHR samples was found to be 20 and 79 °C, respectively. Although CHR showed the least soot oxidation temperature in the first cycle, but it almost reached the activity of CHM after five cycles of reactions. Thus, the catalytic stability in terms of reusability properties, CHM exhibited better than CHR because the CHM can self-regenerate its structure in each cycle. Nonetheless, CHR was less reversible and clusters of RuO_2 on nano-flakes of CeO_2 became inactive on the surface after reduction with carbon, which successively decreased the formation of active oxygen species (O_2^-)/(O_2^{2-}) after a few soot oxidation reactions. Thus, CHR showed a significant loss in catalytic

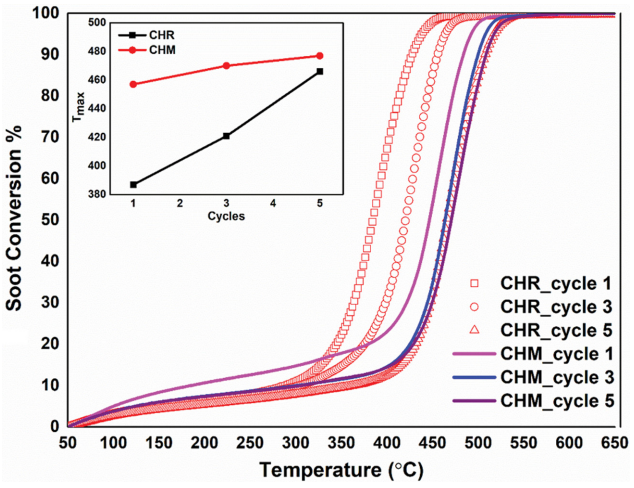

Fig. 12. Reusability studies - five consecutive soot oxidation experiments over the catalysts.

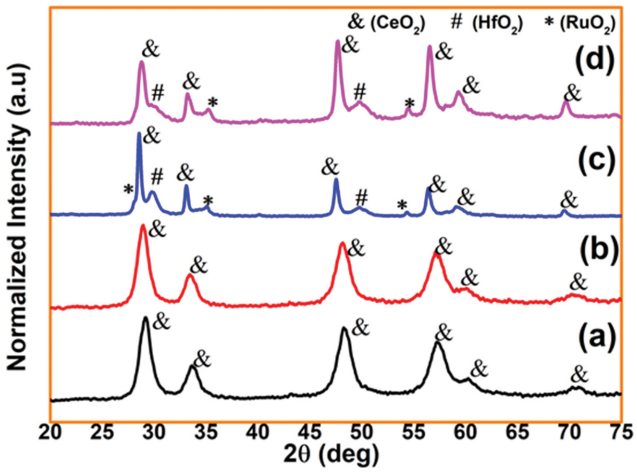

Fig. 13. XRD profiles of the mixed oxides (a) CHM_fresh, (b) CHM_spent (c) CHR_fresh and (d) CHR_spent.

activity after five cycles of reaction.

Furthermore, to understand the structural stability XRD was recorded for the spent catalysts as shown in Fig. 13; hereafter, the used catalysts were designated as CHR_spent and CHM_spent and its profiles were compared with the fresh catalysts. The peaks of the CHM_spent sample are well-matched with the fresh sample and no extra peaks were detected. It preserved the original structure. However, for CHR, the intensity of the diffraction peaks was tremendously decreased, indicating there was a huge loss of crystallinity after five cycles of reactions. Also, RuO_2 peaks were noticed at around 35.24° and 54.48°, and the HfO_2 peaks observed at 30.16° and 49.86°, indicating there was no loss of RuO_2 and HfO_2 from the surface after five cycles of the soot oxidation reaction. However, the secondary phase oxide peaks were shifted to higher angles, which might due to the shrinkage of oxides after five consecutive heat treatments. Thus, CHR showed a huge loss of its catalytic activity ($\Delta T_{cycle\,5}-\Delta T_{cycle\,1}$=79 °C), as discussed earlier in Fig. 12, but the sample CHM showed considerable catalytic loss ($\Delta T_{cycle\,5}-\Delta T_{cycle\,1}$=20 °C) because of good phase stability and regeneration capability even after five cycles of the soot oxidation reaction.

HETEROGENEOUS (SOOT-CATALYST-OXYGEN) REACTION MECHANISM

Based on the above results, the proposed oxidation mechanism on the surface of the doped samples (CH, CHM) and the RuO_2/HfO_2 deposited CeO_2 (CHR) is shown in Fig. 14. CH and CHM samples showed oxygen vacancies (represented as □) as evidenced through Raman spectroscopy. Further, Ce^{4+} reduced to Ce^{3+} (evidenced by H_2-TPR), which promotes the formation of surface-oxygen vacancies as step I. The molecular oxygen (O_2) adsorbs onto the surface vacancy (□) by van der Waals forces [55], as a step II. Subsequently, the reduced Ce^{3+} interacts with the vacancy filled molecular oxygen by transferring an electron to O_2 and produces a reactive superoxide anion (O_2^-) approximately at around 290°C (evidenced in O_2-TPD). Further, one more electron transfers from the surface convert superoxide (O_2^-) to peroxide (O_2^{2-})

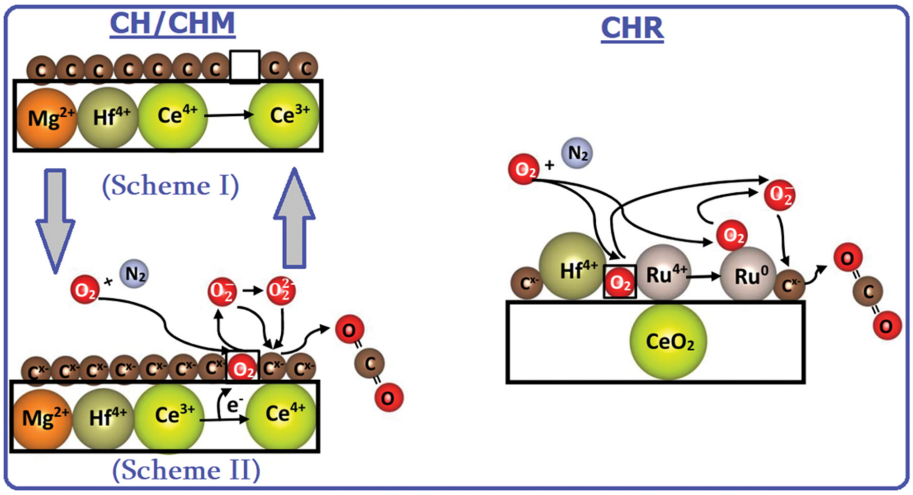

Fig. 14. Soot oxidation mechanism over doped samples (CH and CHM) and the un-doped CHR sample.

approximately at around 350-400°C (evidenced in O_2-TPD). Thus, the formed charged anionic species O_2^- and O_2^{2-} are highly reactive towards the activated soot nano-particles as step III. After the reaction, it forms CO_2 gas and is left □ on the surface and the catalyst can enable re-oxidized Ce^{3+} to Ce^{4+}, as a step II. Thus, this typical cycle of the soot oxidation pathway occurs in the range of 250 to 500 °C, the temperature at which the formation of reactive oxygen species occurs due to the redox coupling of ceria.

In the CHR sample, the possible reaction mechanism occurs in two pathways: (i) the reaction around the Ru-species, and (ii) the reaction occurs at the surface interfacial area provided by the weak interactions of Ce-O-Ru. Furthermore, it evidenced the □ on the surface (Raman spectroscopy) due to successive reductions of Ru^{4+} to metallic Ru and also ceria reduction around Ru species (100-120 °C, H_2-TPR), promotes oxygen vacancies as a step (i and iv). It also evidenced O_2^- species through O_2-TPD analysis. Further, the molecular oxygen adsorbed onto the surface vacancies as shown in steps (ii and v) and converted into superoxide O_2^- by transferring an electron either from Ru-O-Ru or Ru-O-Ce atoms. However, further conversion of superoxide to peroxide was not evidenced in this sample (O_2-TPD) because of the fewer vacancies □ on the surface. In steps (iii and vi), the active superoxide O_2^- reacted with activated soot particles and thus formed CO_2 gas, leaving a vacancy on the surface. Nonetheless, this catalyst possesses less self-regenerative activity due to fewer vacancies on the surface of CeO_2. Thus, the active compound in CHR is RuO_2 in which weakly bounded O^{2-} close to Ce-O-Ru enhance the formation of O_2^-; however, this leads to a decline in activity after certain cycles of soot oxidation reactions.

A. Mechanism over binary Oxide (Hf^{4+} doped CeO_2)

The step by step soot oxidation reactions on the doped sample (CH).

Step I: $Ce^{4+}-O-Hf^{4+} \rightarrow Ce^{3+}-\square-Hf^{4+}$

Step II: $Ce^{3+}-\boxed{O_2}-Hf^{4+} \rightarrow Ce^{4+}-O_2^-/O_2^{2-}-Hf^{4+}$

Step III: $Ce^{4+}-O_2^-/O_2^{2-}-Hf^{4+}+C^{x-} \rightarrow Ce^{3+}-\square-Hf^{4+}+O=C=O$

B. Mechanism over ternary oxide (Hf^{4+}, Mg^{2+} doped CeO_2)

The step by step soot oxidation reactions over CHM sample.

Step I: $Ce^{4+}-O-Mg^{2+}/Hf^{4+} \rightarrow Ce^{3+}-\square-Mg^{2+}/Hf^{4+}$

Step II: $Ce^{3+}-\boxed{O_2}-Mg^{2+}/Hf^{4+} \rightarrow Ce^{4+}-O_2^-/O_2^{2-}-Mg^{2+}/Hf^{4+}$

Step III: $Ce^{4+}-O_2^-/O_2^{2-}-Mg^{2+}/Hf^{4+}+C^{x-}$
$\rightarrow Ce^{3+}-\square-Mg^{2+}/Hf^{4+}+O=C=O$

C. Mechanism over deposited HfO_2/RuO_2 on CeO_2

The soot oxidation reaction steps on the un-doped sample (CHR) occur in two pathways as shown in C.1 and C.2.

C.1. Reaction around Ru-species

Step (i): $Ru^{4+}-O-Ru^{4+} \rightarrow Ru^0-\square-Ru^0$

Step (ii): $Ru^0-\boxed{O_2}-Ru^0 \rightarrow Ru^{4+}-O_2^-Ru^{4+}$

Step (iii): $Ru^{4+}-O_2^-Ru^{4+}+C^{x-} \rightarrow Ru^0-\square-Ru^0+O=C=O$

C.2. Reaction at the interface (surface ceria around Ru species, Ce^{4+}-O-Ru^{4+})

Step (iv): $Ce^{4+}-O-Ru^{4+} \rightarrow Ce^{3+}-\square-Ru^0$

Step (v): $Ce^{3+}-\boxed{O_2}-Ru^0 \rightarrow Ce^{4+}-O_2^-Ru^{4+}$

Step (vi): $Ce^{4+}-O_2^-Ru^{4+}+C^{x-} \rightarrow Ce^{3+}-\square-Ru^0+O=C=O$

CONCLUSIONS

The binary oxide CH (doped Hf in CeO_2) and ternary mixed oxides CHR (undoped Hf/Ru in CeO_2), and CHM (doped Hf/Mg in CeO_2) were studied for soot oxidation experiments. The prepared catalysts were investigated for in-depth surface properties using XRD, FESEM/EDS, TEM, Raman, H_2-TPR, O_2-TPD, XPS and soot-TPR. The dopants Hf^{4+}, Mg^{2+} were successfully incorporated into the ceria lattice and exerted lattice contraction; however, CHR exhibited secondary phases tetragonal (RuO_2) and orthorhombic (HfO_2) deposited onto the cubic fluorite phase because of significant difference in their ionic sizes. The deposited phases also

evidenced through FESEM and TEM images with particle sizes of RuO_2 and HfO_2 were around ~9 to 15 nm. The doped samples (CH and CHM) exhibited higher oxygen vacancies (□) when compared with un-doped CHR. XPS revealed the presence of Ce^{3+}/Ce^{4+}, Hf^{4+}, Mg^{2+}, Ru^0/Ru^{4+} species on the surface of catalysts. H_2-TPR evidenced that the doped samples exhibited ceria reduction (Ce^{4+} to Ce^{3+}) at 300-500 °C. While CHR showed the lower temperature reduction peaks at around 109 °C and 119 °C, attributed to the reduction of surface Ru and the Ce-O-Ru species. In addition, O_2-TPD revealed that the total quantity of actively participating surface chemisorbed oxygen species O_2^- or O_2^{2-} was found to be 0.028, 0.168 and 0.067 mmol·g^{-1} for the samples CH, CHM, and CHR, respectively. Moreover, the ternary mixed oxides CHM and CHR exhibited higher ξ_values than the binary oxide CH. Among the prepared samples, the CHR exhibited lower soot oxidation temperature as compared with the CH/CHM. However, CHR showed a significant loss in activity after five reactions. While CHM showed to be catalytically and structurally stable even after five cycles of soot oxidation reactions.

ACKNOWLEDGEMENTS

This work is supported by the Department of Science and Technology - Science and Engineering Research Council, India (DST SERB: EMR/2016/002598). The authors would like to acknowledge MRC, MNITJ for conducting Raman, TEM, and XPS analysis.

SUPPORTING INFORMATION

Additional information as noted in the text. This information is available via the Internet at http://www.springer.com/chemistry/journal/11814.

REFERENCES

1. J. Oi-Uchisawa, A. Obuchi, A. Ogata, R. Enomoto and S. Kushiyama, *Appl. Catal. B Environ.*, **21**, 9 (1999).
2. G. Yu, J. Wang, J. Liu, X. Cheng, H. Ma, H. Wu, Z. Yang, G. Zhang and X. Sun, *Catal. Lett.*, **149**, 3543 (2019).
3. H. He, X. Lin, S. Li, Z. Wu, J. Gao, J. Wu, W. Wen, D. Ye and M. Fu, *Appl. Catal. B Environ.*, **223**, 134 (2018).
4. H. Zhang, W. Hu, C. Zhou, H. Liu, P. Yao, J. Wang and Y. Chen, *Appl. Catal. A Gen.*, **563**, 204 (2018).
5. M. Piumetti, T. Andana, S. Bensaid, D. Fino, N. Russo and R. Pirone, *AIChE J.*, **63**, 216 (2017).
6. L. Urán, J. Gallego, W. Y. Li and A. Santamaría, *Appl. Catal. A Gen.*, **569**, 157 (2019).
7. F. Fang, N. Feng, L. Wang, J. Meng, G. Liu, P. Zhao, P. Gao, J. Ding, H. Wan and G. Guan, *Appl. Catal. B Environ.*, **236**, 184 (2018).
8. G. Zhai, J. Wang, Z. Chen, S. Yang and Y. Men, *J. Hazard. Mater.*, **363**, 214 (2019).
9. J. Tan, Y. Wei, Y. Sun, J. Liu, Z. Zhao, W. Song, J. Li and X. Zhang, *J. Ind. Eng. Chem.*, **63**, 84 (2018).
10. V. Alcalde-Santiago, A. Davó-Quiñonero, D. Lozano-Castelló and A. Bueno-López, *Appl. Catal. B Environ.*, **234**, 187 (2018).
11. C. Lee, Y. Jeon, S. Hata, J. I. Park, R. Akiyoshi, H. Saito, Y. Teraoka, Y. G. Shul and H. Einaga, *Appl. Catal. B Environ.*, **191**, 157 (2016).
12. S. Liu, X. Wu, W. Liu, W. Chen, R. Ran, M. Li and D. Weng, *J. Catal.*, **337**, 188 (2016).
13. B. Cui, S. Yan, Y. Xia, K. Li, S. Li, D. Wang, Y. Ye and Y. Q. Liu, *Appl. Catal. A Gen.*, **578**, 20 (2019).
14. T. Andana, M. Piumetti, S. Bensaid, N. Russo and D. Fino, *Appl. Catal. A Gen.*, **583**, 117136 (2019).
15. W. Zhang, X. Niu, L. Chen, F. Yuan and Y. Zhu, *Sci. Rep.*, **6**, 1 (2016).
16. S. Bensaid, N. Russo and D. Fino, *Catal. Today*, **216**, 57 (2013).
17. B. Li, A. Raj, E. Croiset and J. Z. Wen, *Catalysts*, **9**, 20 (2019).
18. Y. Hu, X. Yang, S. Cao, J. Zhou, Y. Wu, J. Han, Z. Yan and M. Zheng, *Appl. Surf. Sci.*, **400**, 148 (2017).
19. P. Venkataswamy, D. Jampaiah, K. N. Rao and B. M. Reddy, *Appl. Catal. A Gen.*, **488**, 1 (2014).
20. Y. Cheng, W. Song, J. Liu, H. Zheng, Z. Zhao, C. Xu, Y. Wei and E. J. M. Hensen, *ACS Catal.*, **7**, 3883 (2017).
21. S. Liu, X. Wu, J. Tang, P. Cui, X. Jiang, C. Chang, W. Liu, Y. Gao, M. Li and D. Weng, *Catal. Today*, **281**, 454 (2017).
22. H. Zhao, X. Zhou, M. Wang, Z. Xie, H. Chen and J. Shi, *RSC Adv.*, **7**, 3233 (2017).
23. A. P. Anantharaman, H. P. Dasari, H. Dasari and G. U. B. Babu, *Appl. Catal. A Gen.*, **566**, 181 (2018).
24. T. Melchiori, L. Di Felice, N. Mota, R. M. Navarro, J. L. G. Fierro, M. Van Sint Annaland and F. Gallucci, *Appl. Catal. A Gen.*, **486**, 239 (2014).
25. D. Laishram, K. P. Shejale, R. Gupta and R. K. Sharma, *ACS Sustain. Chem. Eng.*, **6**, 11286 (2018).
26. H. Zhao, X. Hu, J. Hao, N. Li, K. Zhi, R. He, Y. Wang, H. Zhou and Q. Liu, *Appl. Catal. A Gen.*, **591**, 117378 (2020).
27. M. Dhakad, D. Fino, S. S. Rayalu, R. Kumar, A. Watanabe, H. Haneda, S. Devotta, T. Mitsuhashi and N. Labhsetwar, *Top. Catal.*, **42-43**, 273 (2007).
28. K. Simmance, D. Thompsett, W. Wang and B. Thiebaut, *Catal. Today*, **320**, 40 (2019).
29. K. M. Koczkur, S. Mourdikoudis, L. Polavarapu and S. E. Skrabalak, *Dalt. Trans.*, **44**, 17883 (2015).
30. S. Liu, X. Wu, D. Weng and R. Ran, *J. Rare Earths*, **33**, 567 (2015).
31. T. Baidya, M. S. Hegde and J. Gopalakrishnan, *J. Phys. Chem. B*, **111**, 5149 (2007).
32. D. Mukherjee, B. G. Rao and B. M. Reddy, *Appl. Catal. B Environ.*, **197**, 105 (2016).
33. I. Lucentini, A. Casanovas and J. Llorca, *Int. J. Hydrogen Energy*, **44**, 12693 (2019).
34. H. P. Kumar, S. Vidya, S. S. Kumar, C. Vijayakumar, S. Solomon and J. K. Thomas, *J. Asian Ceram. Soc.*, **3**, 64 (2015).
35. L. G. Cruz, J. C. Baglio, V. Siracusano, S. Antonucci, V. Aricò, A. S. Ornelas, R. Ortiz-Frade, L. Osorio-Monreal, G. Durón-Torres and S. M. Arriaga, *Int. J. Electrochem. Sci.*, **6**, 6607 (2011).
36. V. Panić, A. Dekanski, G. Wang, M. Fedoroff, S. Milonjić and B. Nikolić, *J. Colloid Interface Sci.*, **263**, 68 (2003).
37. A. P. Anantharaman, H. P. Dasari, J. H. Lee, H. Dasari and G. U. B. Babu, *Catal. Lett.*, **147**, 3004 (2017).
38. S. Yang, J. Wang, W. Chai, J. Zhu and Y. Men, *Catal. Sci. Technol.*, **9**, 1699 (2019).
39. T. Yi, Y. Zhang and X. Yang, *Appl. Catal. A Gen.*, **570**, 387 (2019).
40. A. E. R. S. Khder, H. M. A. Hassan, M. A. Betiha, K. S. Khairou and

A. A. Ibrahim, *React. Kinet. Mech. Catal.*, **112**, 61 (2014).
41. H. Huang, Q. Dai and X. Wang, *Appl. Catal. B Environ.*, **158-159**, 96 (2014).
42. P. C. Liao, C. S. Chen, W. S. Ho, Y. S. Huang and K. K. Tiong, *Thin Solid Films*, **301**, 7 (1997).
43. K. A. Ledwa, L. Kępiński, M. Ptak and R. Szukiewicz, *Appl. Catal. B Environ.*, **274**, 1 (2020).
44. A. Satsuma, M. Yanagihara, J. Ohyama and K. Shimizu, *Catal. Today*, **201**, 62 (2013).
45. T. Vinodkumar, B. G. Rao and B. M. Reddy, *Catal. Today*, **253**, 57 (2015).
46. M. Morales, *Int. J. Green Technol.*, **3**, 51 (2018).
47. H. Zhu, J. Xu, Y. Yichuan, Z. Wang, Y. Gao, W. Liu and H. Yin, *J. Colloid Interface Sci.*, **508**, 1 (2017).
48. B. Jin, Y. Wei, Z. Zhao, J. Liu, Y. Li, R. Li, A. Duan and G. Jiang, *Cuihua Xuebao/Chinese J. Catal.*, **38**, 1629 (2017).
49. X. Wang, J. Ni, B. Lin, R. Wang, J. Lin and K. Wei, *Catal. Commun.*, **12**, 251 (2010).
50. J. Zhang, D. Tan, Q. Meng, X. Weng and Z. Wu, *Appl. Catal. B Environ.*, **172-173**, 18 (2015).
51. X. C. Hu, X. P. Fu, W. W. Wang, X. Wang, K. Wu, R. Si, C. Ma, C. J. Jia and C. H. Yan, *Appl. Catal. B Environ.*, **268**, 118424 (2020).
52. F. Wang, C. Li, X. Zhang, M. Wei, D. G. Evans and X. Duan, *J. Catal.*, **329**, 177 (2015).
53. H. P. Uppara, J. S. Pasuparthy, S. Pradhan, S. K. Singh, N. K. Labhsetwar and H. Dasari, *Mol. Catal.*, **482**, 110665 (2020).
54. Q. Dai, S. Bai, Z. Wang, X. Wang and G. Lu, *Appl. Catal. B Environ.*, **126**, 64 (2012).
55. J. He, W. H. Fang, R. Long and O. V. Prezhdo, *J. Am. Chem. Soc.*, **141**, 5798 (2019).

Supporting Information

The catalytic activity of Ce-Hf, Ce-Hf-Mg mixed oxides and RuO_2/HfO_2 deposited on CeO_2: Role of superoxide/peroxide in soot oxidation reaction

Hari Prasad Uppara*, Sunit Kumar Singh, Nitin Kumar Labhsetwar**, Mudiyaru Subrahmanya Murari***, and Harshini Dasari*,†**

*Department of Chemical Engineering, Manipal Institute of Technology, Manipal Academy of Higher Education, Manipal, 576104, India
**Energy and Resource Management Division, CSIR-National Environmental Engineering Research Institute, Nagpur, 440 020, Maharashtra, India
***DST-PURSE Program, Mangalore University, Mangalagangotri-574199, India
(*Received 28 January 2021 • Revised 23 March 2021 • Accepted 11 April 2021*)

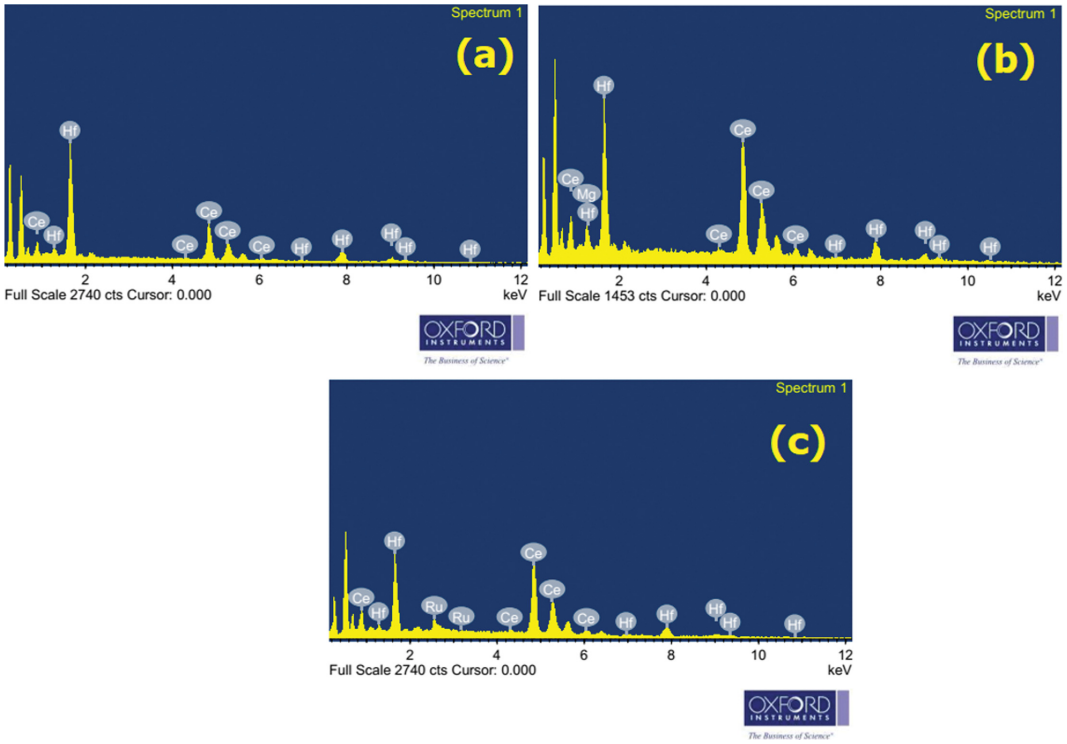

Fig. S1. EDS analysis of the samples (a) CH, (b) CHM and (c) CHR.

Table S1. Elemental composition of the samples

S. No	Nominal composition Ce : Hf : X	Composition from EDS analysis Ce : Hf : X
CH	0.5 : 0.5	0.502 : 0.497
CHM	0.6 : 0.3 : 0.1	0.651 : 0.286 : 0.061
CHR	0.6 : 0.3 : 0.1	0.66 : 0.255 : 0.080

Note: X=Mg and Ru atoms in CHM and CHR samples respectively.

Table S2. The binding energies of Ce3d and the corresponding fitted peak areas (XPS analysis)

S. No	Peak notation	CH		CHM		CHR	
		B.E (eV)	Area	B.E (eV)	Area	B.E (eV)	Area
1	V_o	880.0	1,246.9	879.6	426.1	879.7	6,427.8
2	V	881.9	5,162.0	881.6	7,249.2	881.4	6,815.7
3	V^{I}	885.4	8,187.0	885.5	19,109.0	884.7	20,451.3
4	V^{II}	889.4	732.9	890.9	118.9	888.6	774.4
5	V^{III}	897.0	584.2	898.0	1,380.5	896.5	1,008.7
6	u_o	898.5	3,156.2	900.1	1,212.0	897.7	3,964.6
7	u	900.6	1,992.2	900.1	7,381.3	899.6	8,002.7
8	u^{I}	903.5	5,912.3	904.4	11,054.4	903.2	10,711.1
9	u^{II}	907.5	1,027.3	909.2	60.4	906.5	1,810.7
10	u^{III}	916.4	1,684.7	916.6	2,788.1	915.8	2,741.3
Reduction (R)		0.62		0.63		0.66	

Note: The concentration of Ce^{3+} or reduction (R) is determined by the following equation.

$$\text{Reduction (R)} = \frac{Ce^{3+}}{Ce^{3+}Ce^{4+}} = \frac{Vo + v' + uo + u'}{\text{Total}}$$

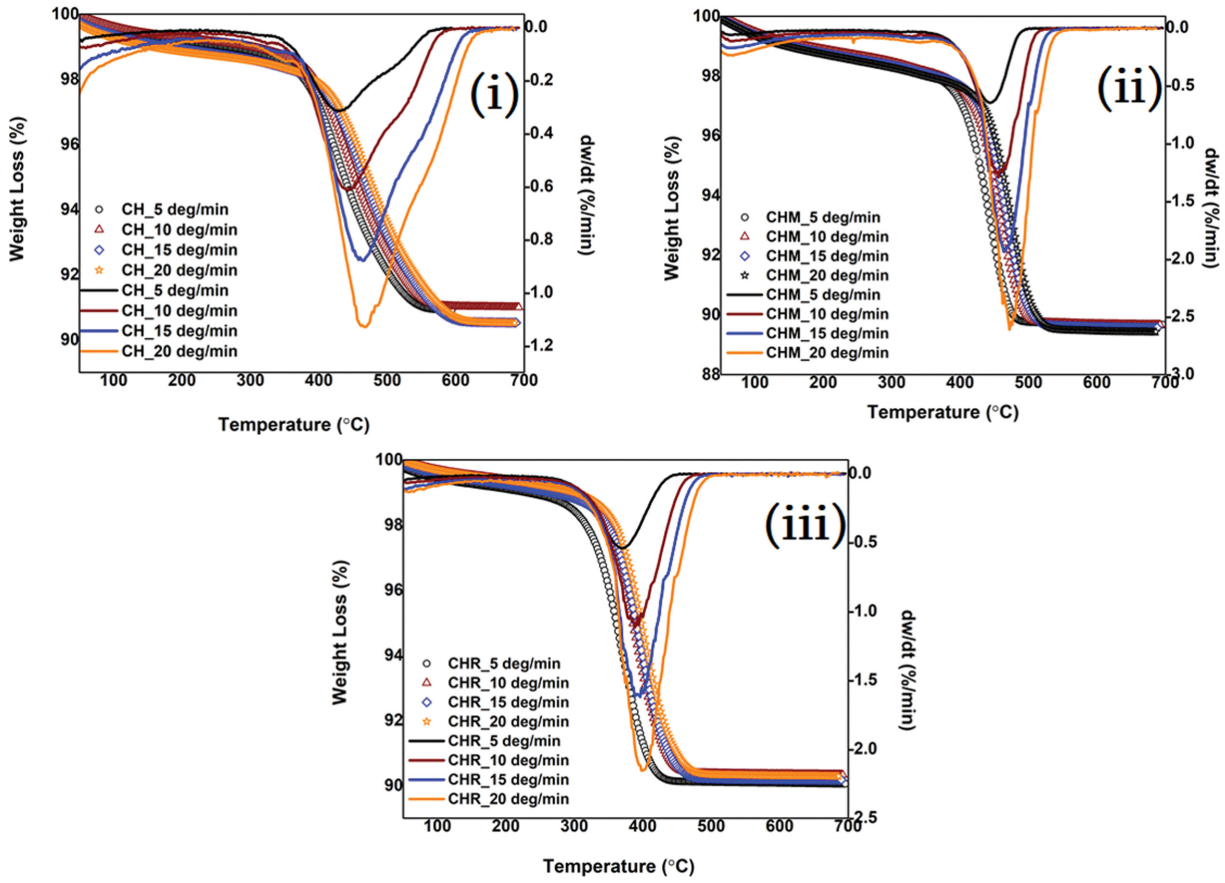

Fig. S2. Soot oxidation under 5%O_2+N_2 at different heating rates (5, 10, 15 and 20 °C/min); (i) CH, (ii) CHM, (iii) CHR.

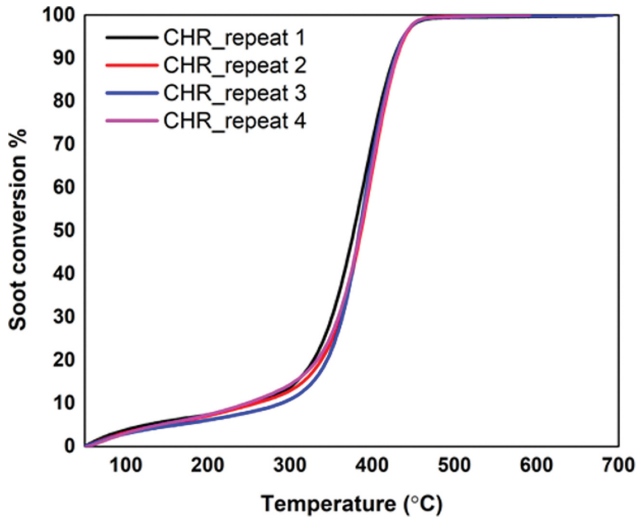

Fig. S3. The CHR sample carried four repeated soot oxidation experiments under 5%O_2+N_2 atmosphere.